
Article:
Wu, L.J., Li, Z., Huang, X. et al. (3 more authors) (2018) A hybrid field model for open-circuit field prediction in surface-mounted PM machines considering saturation. IEEE Transactions on Magnetics, 54 (6). 8103812. ISSN 0018-9464

https://doi.org/10.1109/TMAG.2018.2817178

A Hybrid Field Model for Predicting On-Load Field in Surface-Mounted Permanent-Magnet Machines Considering Saturation

L. J. Wu[1], *Senior Member IEEE*, Zhaokai Li[1], Dong Wang[2], *Member IEEE*, Xiaoyan Huang[1], *Member IEEE*, and Z. Q. Zhu[3], *Fellow IEEE*

[1]College of Electrical Engineering, Zhejiang University, Hangzhou, 310027 China
[2]National Key Laboratory of Science and Technology on Vessel Integrated Power System
Naval Univ. of Engineering, 430000, Wuhan, China
[3]Department of Electronic and Electrical Engineering, University of Sheffield, Sheffield S1 3JD, U.K.

A hybrid field model (HFM) considering saturation effect is presented for predicting the on-load magnetic field distribution in surface-mounted permanent-magnet (SPM) machines, which combines complex permeance model (CPM) and magnetic equivalent circuit (MEC). In the proposed model, MEC calculates the magnetic potential distribution on the stator bore, which is transformed into equivalent current to account for saturation effect. Moreover, local magnetic saturation of tooth-tip is also transformed into equivalent current on the tooth surface. A solving procedure is proposed to calculate the equivalent current and guarantee the convergence. Compared with CPM, the proposed model considering saturation effect significantly improves the prediction accuracy of the on-load performance. The finite element predictions and experimental results demonstrate the excellent accuracy of the HFM predictions.

***Index Terms*—Analytical model, magnetic equivalent circuit, complex permeance, saturation effect, SPM machines.**

I. Introduction

PERMANENT-MAGNET (PM) machines have been one of the most popular machines due to high torque density, high efficiency and excellent dynamic performance [1]. Numerical methods, such as finite-element method (FEM), are reliable for accurate prediction of electromagnetic performance and parasitic effects in the PM machines as it can easily account for saturation and complex structures. However, it is very time-consuming and provides little straightforward physical insight for machine design [2].

Meanwhile many analytical models have been developed to reveal the physical relationship between the geometry of PM machines and their performance [3]-[10]. In these models, the air-gap flux density is predicted by solving the Poisson's or Laplace's equations under the assumption of infinite permeability of the iron. Zhu *et al.* calculated the field distribution in the air-gap/magnet regions and introduced the relative permeance function to take account of the slotting effect for radial component of flux density [3]-[5]. Zarko *et al* proposed the complex permeance function based on conformal mapping to describe the stator slotting for both radial and circumferential flux density [6]. Moreover, Boules replaced the PMs with equivalent current sheet on the surface of the magnets and calculated the air-gap flux density by Hague's equation [7]. O'Connell *et al* utilized the Schwarz-Christoffel (SC) transformation to account for slotting effect based on the field solution of Hague's equation [8]. Boughrara *et al.* extended the usage of SC transformation for machines with arbitrarily curved magnet surfaces and predicted air-gap field and torque with high accuracy [9]. Wu *et al.* developed a subdomain model considering the influence of tooth-tips and achieved excellent accuracy for predicting the cogging torque and flux density [10]. However, these models all neglect the nonlinear property of the iron core.

In order to eliminate the error due to saturation effect, some analytical models were developed to consider the magnetic field distribution in the iron region [11]-[14]. The key points of these models are the calculation of the magnetic reluctance in the saturated region. For a specific load, Dalal *et al.* obtained the air-gap field distribution by solving Laplace/quasi-Poissonian equations in six regions, of which the stator core permeability is assumed a linear function of the load angle [11]. However, such linear function is found by using FEM and the whole stator iron is assumed the constant permeability. Liang *et al.* calculated the permeability of saturated iron region using iterative method and derived the analytical solution of saturated region and other subdomains [12]. However, this model only considers the saturation of the magnetic bridge in the rotor. Djelloul-Khedda *et al.* proposed a subdomain model to calculate the magnetic field distribution of switched reluctance machine accounting for the nonlinear permeability of the stator and rotor teeth [13]. However, this model is time-consuming since it needs solving a matrix for each rotor position. Farshadnia *et al.* calculated the relative permeability at different regions of the rotor iron in switched reluctance machine and modified the equivalent air-gap function to predict the air-gap flux density considering saturation effect [14]. However, these models [12]-[14] are not suitable for SPM machines.

On the other hand, MEC is often used to analyze the nonlinear iron core. From the MEC solution, the MMF drops of the stator [15]-[16] or the permeability of the tooth [17] are used to represent the saturation effect by equivalently increasing the air-gap length and slot opening. Then the complex permeance was introduced to account for both saturation effect and slotting effect. Hanic *et al.* combined the conformal mapping and MEC for predicting the air-gap field in the saturated SPM machine [18]-[19]. The additional point wires were introduced in the air-gap which are equal to the magnetic voltage drops across iron to model the saturation effect. However, all models in [15]-[19] are time-consuming due to their usage of SC transformation at every rotor position. In [20], the open-circuit magnetic field of

the saturated SPM machines were accurately predicted based on the combination of CPM and MEC. However, it is not for onload analysis, which is the focus of this paper.

In this paper, a HFM which combines CPM and MEC is presented for the on-load field prediction in SPM machines. As CPM represents the slotting effect and MEC describes the magnetic potential distribution of the stator iron, the proposed model takes advantage of both methods and considers the saturation of stator yoke, tooth body and tooth-tips. Such combination is based on the equivalence between the magnetic potential drop in the stator and virtual current on the stator bore. In order to calculate the virtual current representing saturation effect, a solving procedure based on Newton-Raphson method is developed to guarantee the convergence in the iteration. The on-load FEM analysis and experiment are carried out to validate the proposed model.

II. Hybrid Field Model

Assumptions are made to simplify the problem as follows: 1) linear magnet property with constant relative permeability; 2) all materials are isotropic; 3) no static/dynamic rotor eccentricities; 4) infinitely permeable rotor iron; and 5) negligible end effect.

Fig. 1 shows the schematic view of the slotted SPM machine with tooth-tips in polar coordinates. The saturation of stator yoke and tooth body can be equivalently transformed into the virtual current on the slot opening of the stator bore while tooth-tip saturation is represented as the equivalent current on the tooth surface. Therefore, the nonlinearly permeable iron is transformed to infinately permeable iron with equivalent current on the stator bore in the SPM machine, as shown in Fig. 2.

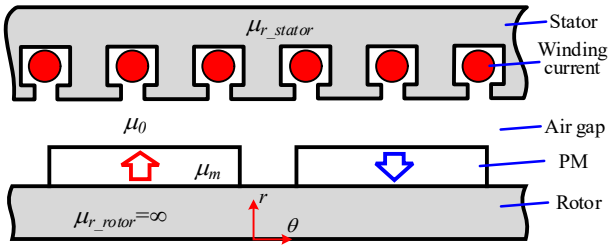

Fig. 1 Schematic view of SPM machine under any load condition in polar coordinates.

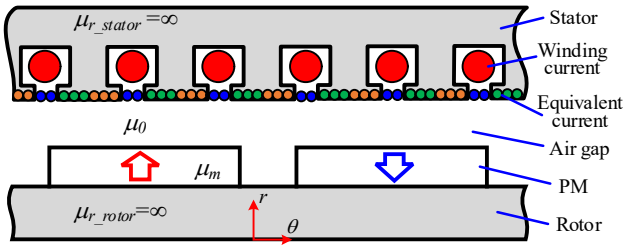

Fig. 2 Hybrid field model of slotted SPM machine considering saturation effect under on-load condition.

A. Equivalent Current Representing Stator Saturation

The equivalent current, which represents saturation effect, is the keypoint in the HFM. It is calculated from the magnetic potential distribution of MEC. Fig. 3 shows that the magnetic reluctances representing the nonlinear property of the stator iron are connected to form the magnetic network. V_1, V_2,$\cdots$,$V_{(6Qs)}$ are the node magnetic potential in the MEC .The air-gap flux φ_j flowing into the stator is expressed as

$$\varphi_j = \int_{s_j} B_{sr} ds \tag{1}$$

where s_j is the area of the slot or tooth on the stator bore, j is the index of the slot and tooth (j=1,2,$\cdots$,$2Q_s$, where Q_s is the total number of slots) and B_{sr} is the radial flux density on the stator bore. The magnetic potential distribution of stator is obtained by solving the MEC in Fig. 3, according to Kirchhoff's law.

$$f(\mathbf{V}) = \mathbf{A}\boldsymbol{\Lambda}(\mathbf{A}^{\mathrm{T}}\mathbf{V} - \mathbf{E}) - \boldsymbol{\Phi} = 0 \tag{2}$$

where $\mathbf{A}$ is the incidence matrix, $\boldsymbol{\Lambda}$ is the branch permeance matrix, $\mathbf{V}$ is the node magnetic potential matrix, $\boldsymbol{\Phi}$ is the node flux matrix on the stator bore which consists of φ_j and $\mathbf{E}$ is the branch MMF matrix calculated by winding current [21]

$$\begin{cases} E_{2Q_s} = E_{Q_s} = -\dfrac{1}{2Q_s}\displaystyle\sum_{n=1}^{Q_s-1}(Q_s - n)i_{wk} \\ E_{Q_s+1} = E_1 = E_{Q_s} + \dfrac{i_{w1}}{2} \\ E_{Q_s+2} = E_2 = E_1 + \dfrac{i_{w2}}{2} \\ \cdots \\ E_{2Q_s-1} = E_{Q_s-1} = E_{Q_s-2} + \dfrac{i_{w(Q_s-1)}}{2} \end{cases} \tag{3}$$

where E_1, E_2,$\cdots$, E_{2Qs} are the values of branch MMF which forms $\mathbf{E}$ and i_{w1}, i_{w2}, ,$\cdots$, $i_{w(Qs-1)}$ are the winding current.

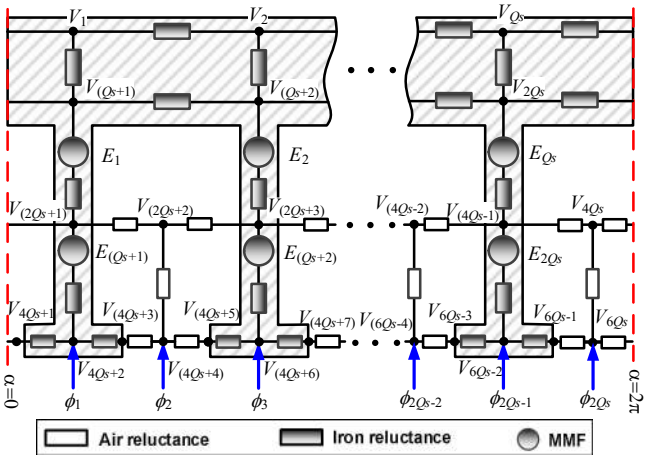

Fig. 3 Equivalent magnetic network of the stator.

The equivalent current on the slot is calculated from the magnetic potential drop of the stator yokes and stator teeth, while the equivalent current on the tooth surface is calculated from the magnetic potential drop of the tooth-tips. This relationship is expressed as

$$\begin{cases} i_{ssk} + i_{wk} = -(V_{m+2} - V_m) \\ i_{tlk} = -(V_{m-1} - V_{m-2}) \\ i_{trk} = -(V_m - V_{m-1}) \end{cases} \tag{4}$$

where i_{ssk} and i_{wk} are the equivalent and winding currents on the kth slot opening, respectively, i_{tlk} and i_{trk} are the equivalent current on the left and right sides of the kth tooth, respectively (k is the index of tooth and slot, k=1,2,⋯,Q_s). They are specified in Fig. 4. V_m represents the magnetic potential on the stator bore, e.g., m=4Q_s+3 in Fig. 3. Hence, equation (4) can also be expressed in matrix form as

$$\begin{cases} \mathbf{I_{ss}} + \mathbf{I_w} = \mathbf{C_{ss}V} \\ \mathbf{I_{tl}} = \mathbf{C_{tl}V} \\ \mathbf{I_{tr}} = \mathbf{C_{tr}V} \end{cases} \tag{5}$$

where $\mathbf{C_{ss}}$, $\mathbf{C_{tl}}$, $\mathbf{C_{tr}}$ are constant matrix calculated from (4) and

$$\mathbf{I_{ss}} = \begin{bmatrix} i_{ss1} & i_{ss2} & \cdots & i_{ssQ_s} \end{bmatrix}^{\mathrm{T}} \tag{6}$$

$$\mathbf{I_w} = \begin{bmatrix} i_{w1} & i_{w2} & \cdots & i_{wQ_s} \end{bmatrix}^{\mathrm{T}} \tag{7}$$

$$\mathbf{I_{tl}} = \begin{bmatrix} i_{tl1} & i_{tl2} & \cdots & i_{tlQ_s} \end{bmatrix}^{\mathrm{T}} \tag{8}$$

$$\mathbf{I_{tr}} = \begin{bmatrix} i_{tr1} & i_{tr2} & \cdots & i_{trQ_s} \end{bmatrix}^{\mathrm{T}} \tag{9}$$

Therefore, the equivalent current can be obtained from (2) and (5).

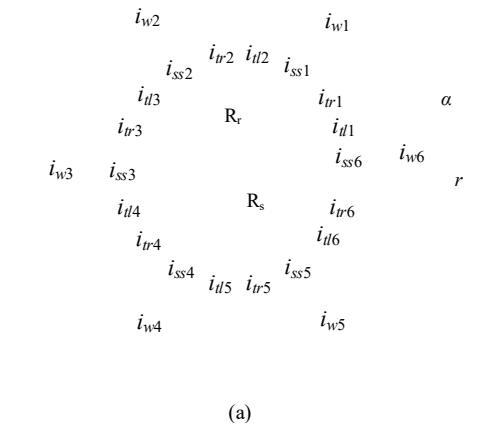

(a)

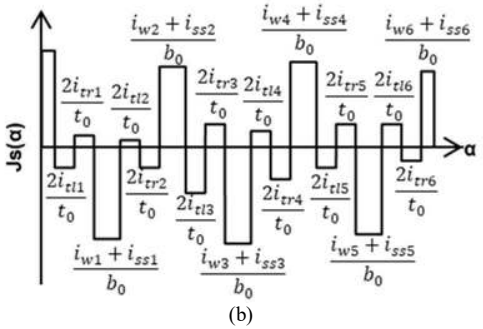

(b)

Fig. 4 Current sheet distribution on the stator bore of the slotless machine (including winding current and stator saturation current)

B. Slotted Air-Gap Field Solution

Since the equivalent current is calculated to represent the saturation effect, the stator iron is considered to have infinite permeability, as shown in Fig. 2. In order to simplify the analytical calculation of air-gap field, the electromagnetic field problem neglecting slotting effect is generalized, as shown in Fig. 5. R_s, R_m, and R_r are the radii of stator bore, magnet outer surface and rotor yoke surface, respectively. J_s is the resultant of winding current and equivalent current of saturation on the stator bore and can be expressed as (10) from Fig. 4.

$$J_s = \begin{cases} \dfrac{i_{wk}-i_{ssk}}{b_0}, & \dfrac{2k\pi}{Q_s} - \dfrac{b_0}{2R_s} \le \alpha \le \dfrac{2k\pi}{Q_s} + \dfrac{b_0}{2R_s} \\ \dfrac{i_{tlk}}{t_0}, & \dfrac{(2k-1)\pi}{Q_s} - \dfrac{t_0}{2R_s} \le \alpha \le \dfrac{(2k-1)\pi}{Q_s} \\ \dfrac{i_{trk}}{t_0}, & \dfrac{(2k-1)\pi}{Q_s} \le \alpha \le \dfrac{(2k-1)\pi}{Q_s} + \dfrac{t_0}{2R_s} \end{cases} \tag{10}$$
$$k = 1,2,\cdots,Q_s$$

where b_0 is the slot-opening, t_0 is the tooth width on the stator bore.

As shown in Fig. 5, the slotless air-gap field is obtained by superposition of the field produced by the PM, winding current and equivalent current of saturation with infinitely permeable iron. The radial and circumferential air-gap field can be expressed as

$$\begin{aligned} B_r(\alpha,r,t) &= B_{mr}(\theta,r) + B_{wr}(\alpha,r,t) + B_{sat\_r}(\alpha,r,t) \\ &= B_{mr}(\theta,r) + B_{cr}(\alpha,r,t) \end{aligned} \tag{11}$$

$$\begin{aligned} B_\alpha(\alpha,r,t) &= B_{m\alpha}(\theta,r) + B_{w\alpha}(\alpha,r,t) + B_{sat\_\alpha}(\alpha,r,t) \\ &= B_{m\alpha}(\theta,r) + B_{c\alpha}(\alpha,r,t) \end{aligned} \tag{12}$$

where $B_{mr}(\theta, r)$ and $B_{m\alpha}(\theta, r)$ are the radial and circumferential field produced by the PM, $B_{wr}(\alpha, r, t)$ and $B_{w\alpha}(\alpha, r, t)$ are the radial and circumferential field produced by the winding current, $B_{sat\_r}(\alpha, r, t)$ and $B_{sat\_\alpha}(\alpha, r, t)$ are the radial and circumferential field produced by the equivalent current. α is the stator angular position with reference to the axis of phase A winding, θ is the rotor angular position with reference to the axis of a magnet pole and θ=$\omega_r t$+θ_0, where θ_0 is the initial rotor position and ω_r is the mechanical angular velocity.

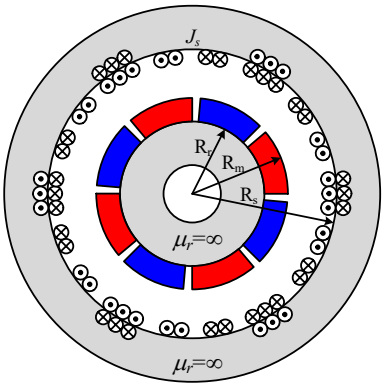

Fig. 5 Hybrid field model of slotless SPM machine.

The solution of the slotless air-gap field produced by PMs neglecting saturation effect was derived in Appendix [22]. Therefore this paper only gives the final expressions of radial and circumferential air-gap flux density

$$B_{mr}(\theta,r) = \sum_{n=1,3,5,\cdots}^{\infty} K_B(n) f_{Br}(r) \cos(np\theta) \tag{13}$$

$$B_{m\alpha}(\theta,r) = \sum_{n=1,3,5,\cdots}^{\infty} K_B(n) f_{B\theta}(r) \sin(np\theta) \tag{14}$$

where $K_B(n)$, $f_{Br}(r)$, and $f_{B\theta}(r)$ are given in Appendix [22].

As for the magnetic field produced by stator current including winding current and equivalent current of saturation

neglecting saturation effect, the governing Laplacian equation in the air-gap region is

$$\frac{\partial^2\varphi}{\partial r^2}+\frac{1}{r}\frac{\partial\varphi}{\partial r}+\frac{1}{r^2}\frac{\partial^2\varphi}{\partial\alpha^2}=0 \tag{15}$$

and the boundary condition is [4]

$$\begin{cases} B_\alpha\big|_{r=R_r}=0 \\ H_\alpha\big|_{r=R_s}=-J_s \end{cases} \tag{16}$$

The Fourier series expansion of the current distribution is obtained as

$$\begin{aligned} J_s=&\sum_{k=1}^{Q_s}\sum_v\frac{2(i_{ssk}+i_{wk})}{\pi b_0}\frac{1}{v}\sin\left(v\frac{b_0}{2R_s}\right)\cos\left[v\left(\alpha-\frac{2k\pi}{Q_s}\right)\right]+\\ &\sum_{k=1}^{Q_s}\sum_v\frac{4i_{tlk}}{\pi t_0}\frac{1}{v}\sin\left(v\frac{t_0}{4R_s}\right)\cos\left[v\left(\alpha-\frac{(2k-1)\pi}{Q_s}+\frac{t_0}{4R_s}\right)\right]+\\ &\sum_{k=1}^{Q_s}\sum_v\frac{4i_{trk}}{\pi t_0}\frac{1}{v}\sin\left(v\frac{t_0}{4R_s}\right)\cos\left[v\left(\alpha-\frac{(2k-1)\pi}{Q_s}-\frac{t_0}{4R_s}\right)\right] \end{aligned} \tag{17}$$

By solving the governing Laplacian equation with the boundary condition, the radial and circumferential components of the magnetic field produced by the stator current are obtained as

$$\begin{aligned} B_{cr}=&\frac{\mu_0}{\pi}\sum_{k=1}^{Q_s}\sum_v\left\{\frac{i_{ssk}+i_{wk}}{v}K_{sov}(b_0)F_v(r)\sin\left[v\left(\alpha-\frac{2k\pi}{Q_s}\right)\right]+\right.\\ &\frac{i_{tlk}}{v}K_{sov}(\frac{t_0}{2})F_v(r)\sin\left[v\left(\alpha-\frac{(2k-1)\pi}{Q_s}+\frac{t_0}{4R_s}\right)\right]+\\ &\left.\frac{i_{trk}}{v}K_{sov}(\frac{t_0}{2})F_v(r)\sin\left[v\left(\alpha-\frac{(2k-1)\pi}{Q_s}-\frac{t_0}{4R_s}\right)\right]\right\} \end{aligned} \tag{18}$$

$$\begin{aligned} B_{c\alpha}=&\frac{\mu_0}{\pi}\sum_{k=1}^{Q_s}\sum_v\left\{\frac{i_{ssk}+i_{wk}}{v}K_{sov}(b_0)G_v(r)\cos\left[v\left(\alpha-\frac{2k\pi}{Q_s}\right)\right]+\right.\\ &\frac{i_{tlk}}{v}K_{sov}(\frac{t_0}{2})G_v(r)\cos\left[v\left(\alpha-\frac{(2k-1)\pi}{Q_s}+\frac{t_0}{4R_s}\right)\right]+\\ &\left.\frac{i_{trk}}{v}K_{sov}(\frac{t_0}{2})G_v(r)\cos\left[v\left(\alpha-\frac{(2k-1)\pi}{Q_s}+\frac{t_0}{4R_s}\right)\right]\right\} \end{aligned} \tag{19}$$

where μ_0 is the permeability of free space. F_v, G_v, and K_{sov} are given by

$$F_v(r)=\frac{v}{r}\left(\frac{r}{R_s}\right)^v\frac{1+\left(R_r/r\right)^{2v}}{1-\left(R_r/R_s\right)^{2v}} \tag{20}$$

$$G_v(r)=\frac{v}{r}\left(\frac{r}{R_s}\right)^v\frac{1-\left(R_r/r\right)^{2v}}{1-\left(R_r/R_s\right)^{2v}} \tag{21}$$

$$K_{sov}(\beta)=\frac{\sin\left(v\beta/2R_s\right)}{v\beta/2R_s} \tag{22}$$

For the slotted SPM machines, CPM based on the conformal mapping is introduced to account for slotting effect [6]. The complex permeance function is calculated only once in the whole prediction procedure because it completely depends on the slot geometry and airgap length. Thus the radial and circumferential components of the flux density in the slotted air-gap are obtained from those in the slotless air-gap [6]

$$\begin{aligned} B_{sr}&=B_r\lambda_r+B_\alpha\lambda_i \\ B_{s\alpha}&=B_\alpha\lambda_r-B_r\lambda_i \end{aligned} \tag{23}$$

where λ_r and λ_i are the real and imaginary components of complex permeance, respectively. The calculation of λ_r and λ_i are described in Appendix [6].

C. Convergent Solving Procedure

In the proposed HFM, the air-gap field solution and calculation of equivalent current depend on each other. Therefore, a solving procedure is proposed to iteratively calculate the equivalent current as well as air-gap field and guarantee the convergence in one loop. The basic idea is to incorporate the air-gap analytical solution into the procedure of solving the MEC. Therefore, in the MEC, the air-gap flux φ_j flowing into the stator is rederived from (1)

$$\begin{aligned} \varphi_j=&\sum_{k=1}^{Q_s}\left[g_{ssk}(s_j)(i_{ssk}+i_{wk})+g_{tlk}(s_j)i_{tlk}\right.\\ &\left.+g_{trk}(s_j)i_{trk}\right]+\int_{s_{jk}}(\lambda_r B_{mr}+\lambda_i B_{m\alpha})ds \\ =&\mathbf{G_{ss}}(s_j)(\mathbf{I_{ss}}+\mathbf{I_w})+\mathbf{G_{tl}}(s_j)\mathbf{I_{tl}}+\mathbf{G_{tr}}(s_j)\mathbf{I_{tr}}+\varphi_m(s_j) \end{aligned} \tag{24}$$

where g_{ssk}, g_{tlk}, and g_{trk} are calculated from (13)-(23) and

$$\mathbf{G_{ss}}(s_j)=\begin{bmatrix} g_{ss1}(s_j) & g_{ss2}(s_j) & \cdots & g_{ssQ_s}(s_j)\end{bmatrix} \tag{25}$$

$$\mathbf{G_{tl}}(s_j)=\begin{bmatrix} g_{tl1}(s_j) & g_{tl2}(s_j) & \cdots & g_{tlQ_s}(s_j)\end{bmatrix} \tag{26}$$

$$\mathbf{G_{tr}}(s_j)=\begin{bmatrix} g_{tr1}(s_j) & g_{tr2}(s_j) & \cdots & g_{trQ_s}(s_j)\end{bmatrix} \tag{27}$$

The equivalent current $\mathbf{I_{ss}}$+$\mathbf{I_w}$, $\mathbf{I_{tl}}$, $\mathbf{I_{tr}}$ in (24) can be calculated from the magnetic potential distribution of MEC according to (5). Thus φ_j in (24) can be expressed as a function of the magnetic potential distribution $\mathbf{V}$.

$$\varphi_j=\left(\mathbf{G_{ss}}(s_j)\mathbf{C_{ss}}+\mathbf{G_{tl}}(s_j)\mathbf{C_{tl}}+\mathbf{G_{tr}}(s_j)\mathbf{C_{tr}}\right)\mathbf{V}+\varphi_m(s_j) \tag{28}$$

It can also be expressed in matrix form as

$$\mathbf{\Phi}=\left(\mathbf{R_{ss}}\mathbf{C_{ss}}+\mathbf{R_{tl}}\mathbf{C_{tl}}+\mathbf{R_{rl}}\mathbf{C_{tr}}\right)\mathbf{V}+\mathbf{\Phi_m} \tag{29}$$

where

$$\mathbf{R_{ss}}=\begin{bmatrix}\mathbf{G_{ss}}(s_1) & \mathbf{G_{ss}}(s_2) & \cdots & \mathbf{G_{ss}}(s_{2Q_s})\end{bmatrix}^{\mathrm{T}} \tag{30}$$

$$\mathbf{R_{tl}}=\begin{bmatrix}\mathbf{G_{tl}}(s_1) & \mathbf{G_{tl}}(s_2) & \cdots & \mathbf{G_{tl}}(s_{2Q_s})\end{bmatrix}^{\mathrm{T}} \tag{31}$$

$$\mathbf{R_{rl}}=\begin{bmatrix}\mathbf{G_{tr}}(s_1) & \mathbf{G_{tr}}(s_2) & \cdots & \mathbf{G_{tr}}(s_{2Q_s})\end{bmatrix}^{\mathrm{T}} \tag{32}$$

$$\mathbf{R_{rl}}=\begin{bmatrix}\mathbf{G_{tr}}(s_1) & \mathbf{G_{tr}}(s_2) & \cdots & \mathbf{G_{tr}}(s_{2Q_s})\end{bmatrix}^{\mathrm{T}} \tag{33}$$

$$\mathbf{\Phi_m}=\begin{bmatrix}\varphi_m(s_1) & \varphi_m(s_2) & \cdots & \varphi_m(s_{2Q_s})\end{bmatrix}^{\mathrm{T}} \tag{34}$$

Thus, according to (2), the general solution for MEC can be obtained by

$$\begin{aligned} f(\mathbf{V})=&\left[\mathbf{A\Lambda A}^{\mathrm{T}}-\left(\mathbf{R_{ss}}\mathbf{C_{ss}}+\mathbf{R_{tl}}\mathbf{C_{tl}}+\mathbf{R_{rl}}\mathbf{C_{tr}}\right)\right]\mathbf{V}\\ &-\mathbf{A\Lambda E}-\mathbf{\Phi_m}=0 \end{aligned} \tag{35}$$

It can be seen from (35) that only branch permeance matrix $\mathbf{\Lambda}$ depends on the magnetic potential distribution, which should be determined iteratively using BH curves. The 'new' MEC

combined with air-gap field solution of CPM can be solved based on Newton-Raphson method. Fig. 6 shows the general flowchart to calculate the equivalent current and magnetic field in the air-gap. Thus only one loop is required to solve the 'new' MEC, which has taken into account the saturation effect and guarantee the convergence.

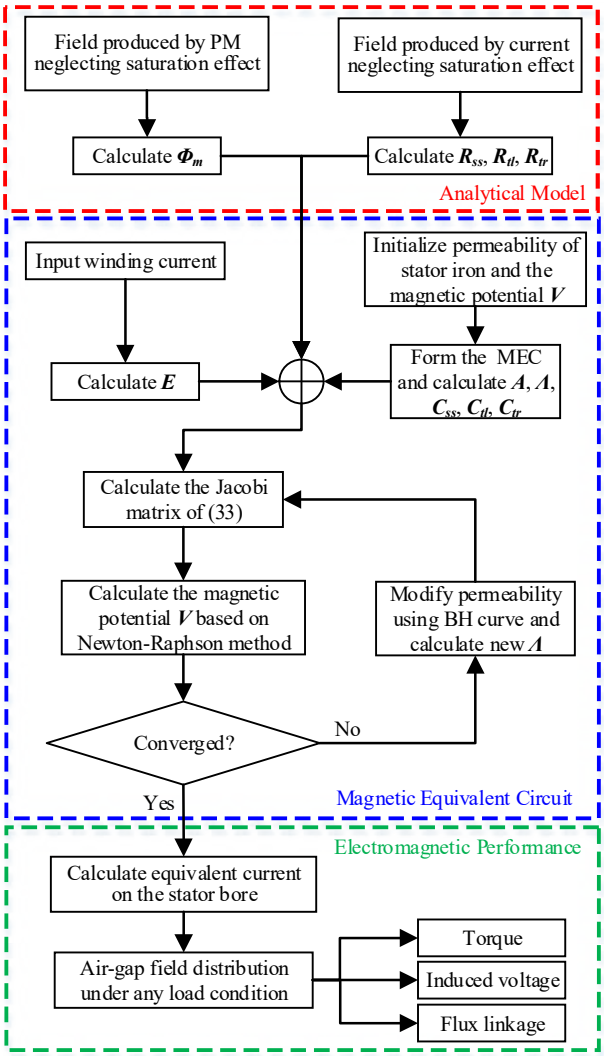

Fig. 6 General flowchart to calculate the magnetic field distribution using convergent calculation procedure.

III. Electromagnetic Performance

When the air-gap field distribution of the SPM machine under on-load condition is predicted, the main flux linking one stator winding coil can be expressed as

$$\varphi_i(t) = R_s l_{ef} \int_{\alpha_i-\tau/2}^{\alpha_i+\tau/2} B_{sr}(\alpha, R_s, t)\, d\alpha \tag{36}$$

where l_{ef} is the effective axial length of a stator coil, α_i and τ represent the angle of axis and coil pitch for one coil of any phase. The total flux linkage includes the slot leakage flux and tooth-tip leakage flux, which can be calculated from MEC. Hence, by summing the flux linkages associated with all coils from the same phase, the total flux linkage ψ_{ph} is obtained by

$$\psi_{ph}(t) = N_c \sum_{i=1}^{\kappa} \left(\varphi_i(t) + \sum_{j=1}^{\gamma} \varphi_{ij}(t) + \sum_{j=1}^{\gamma} \varphi_{(i+\tau)j}(t) \right) \tag{37}$$

where N_c is the number of turns per slot for one phase, κ is the number of the coils of the same phase in different slots, γ is the layer of the tangential magnetic reluctance in one slot, φ_{ij} and $\varphi_{(i+\tau)j}$ is the tangential flux in the slot that covers the coil. Then, the induced voltage is defined as the derivative of the flux linkage with respect to time under on-load condition.

$$U_{ph} = -\frac{d\psi_{ph}}{dt} \qquad ph=A,B,C. \tag{38}$$

When the radial and tangential components of the air-gap flux density are predicted, the total torque of the SPM machine can be calculated by integrating the Maxwell's stress tensor along a circle with a radius of r inside the air-gap [23].

$$T = \frac{1}{\mu_0} l_{ef} r^2 \int_0^{2\pi} B_{sr}(\alpha, r, t) B_{s\alpha}(\alpha, r, t) d\alpha \tag{39}$$

IV. FE and Experimental Validation

In order to validate the proposed model, two integer-slot (8-pole/48-slot) and fractional-slot (8-pole/9-slot) SPM machines are investigated by HFM, CPM, and FEM. TABLE I gives the major parameters of these two machines. Fig. 7 shows the flux density distribution of the integer-slot and fractional-slot SPM machines at rated current, which also illustrates the saturation level of the machines. The 8-pole/48-slot machine is operated in the BLAC mode while the other is in the BLDC mode, Fig. 8. Fig. 9 presents the stator and rotor of 8-pole/9-slot prototype machine, which is used for experimental validation.

TABLE I
Main Parameters of Prototype SPM Machines

Parameter	8-pole/48-slot	8-pole/9-slot	Unit
Stator outer radius	75	50	mm
Stator inner radius	45	26.5	mm
Air-gap length	0.75	1	mm
Magnet thickness	4.5	3	mm
Rotor outer radius	44.25	25.5	mm
Shaft radius	17.5	17.5	mm
Stator yoke height	8	4.4	mm
Active length	75	50	mm
Slot opening	1.5	2	mm
Tooth body width	3.72	8.7	mm
Pole-arc to pole-pitch ratio	1	1	
Magnet remanence	1.26	1.2	T
Relative recoil permeability	1.07	1.05	
Magnetization	Parallel	Parallel	
Rated speed	1500	400	rpm
Number of pole pairs	4	4	
Number of slots	48	9	
Rated current	25	10	A
Lamination material	WG35WW300	Transil300	
Operation mode	BLAC	BLDC	

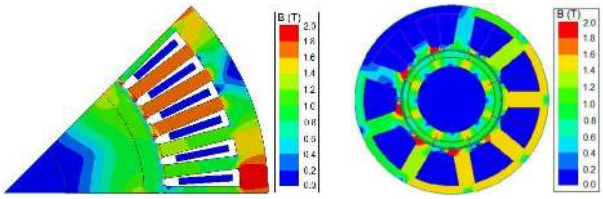

(a) (b)

Fig. 7. Flux density distribution of SPM prototype machines at rated current. (a) 8-pole/48-slot. (b) 8-pole/9-slot.

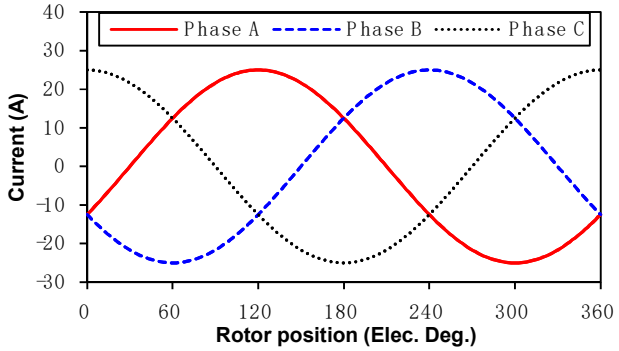

(a)

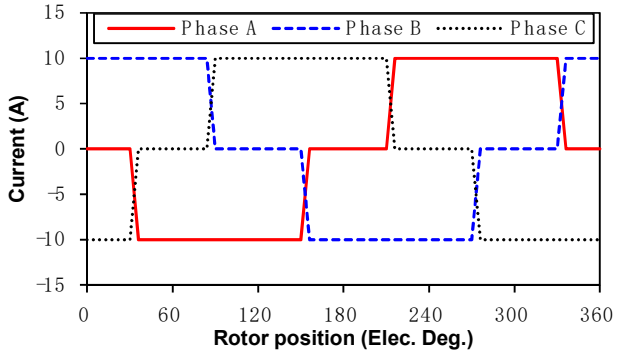

(b)

Fig. 8 The current waveforms of the SPM machines at rated load. (a) 8-pole/48-slot. (b) 8-pole/9-slot.

(a) (b)

Fig. 9 8-pole/9-slot prototype SPM machine. (a) stator.(b) rotor.

When the machines are operating under the rated load, the armature reaction field increases the saturation level and therefore makes the advantage of HFM significant. Figs. 10-11 show that HFM can accurately predict the radial and circumferential components of flux density in the air-gap while CPM always overestimates them due to neglecting saturation effect for both machines. Moreover, the average radial air-gap flux densities, facing the fourth tooth for 8-pole/48-slot machine and facing the seventh tooth for 8-pole/9-slot machine, are predicted by HFM, CPM, and FEM at different peak current, as shown in Figs. 12-13. Radial component of the flux density predicted by HFM agrees well with FEM predictions at different peak current while the flux densities predicted by CPM are much higher than those predicted by FEM, as can be seen in both machines.

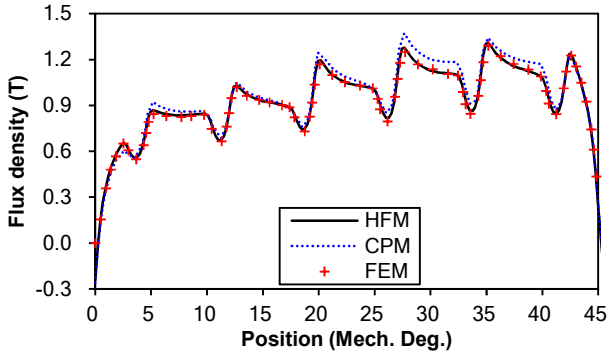

(a)

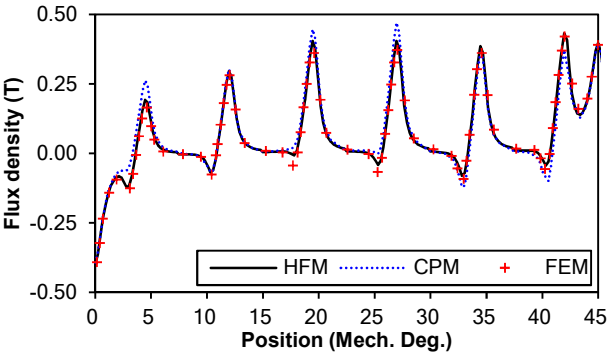

(b)

Fig. 10. HFM, CPM, and FEM predicted air-gap flux density waveforms in the middle of the air-gap of 8-pole/48-slot SPM machine at rated current: (a) radial and (b) circumferential.

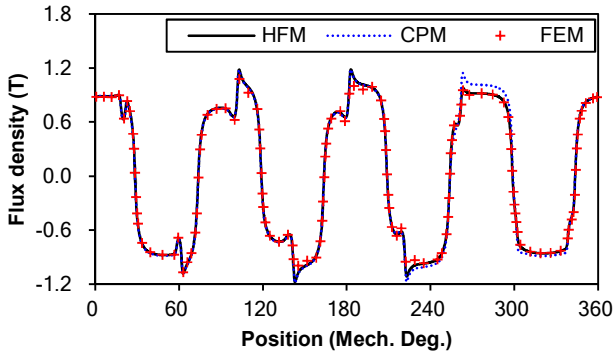

(a)

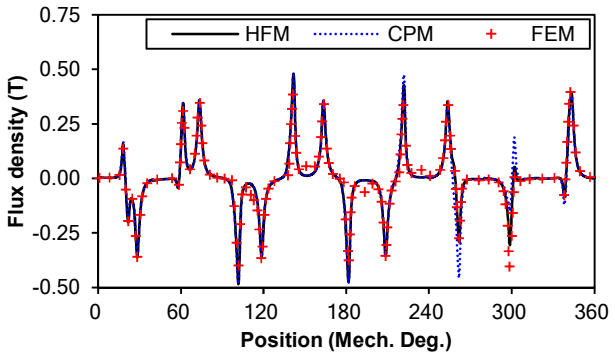

(b)

Fig. 11 HFM, CPM, and FEM predicted air-gap flux density waveforms in the middle of the air-gap of 8-pole/9-slot SPM machine at rated current: (a) radial and (b) circumferential.

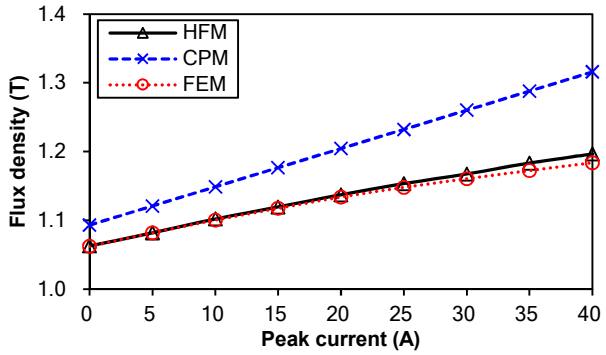

Fig. 12 Variation of average radial airgap flux density facing the fourth tooth with peak current of 8-pole/48-slot SPM machine.

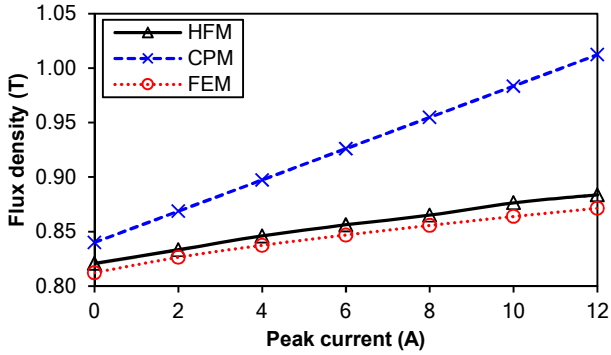

Fig. 13 Variation of average radial airgap flux density facing the seventh tooth with peak current of 8-pole/9-slot SPM machine.

Figs. 14-15 show that HFM can achieve excellent accuracy of flux linkage at rated current while CPM shows low accuracy for both machines. When the machines are under different load condition, the amplitude and phase of the fundamental flux linkage predicted by HFM, CPM and FEM are compared in Figs. 16-17. It can be seen that the amplitude of HFM predicted flux linkage is more accurate than that predicted by CPM. Moreover, the phase error of CPM is increasing rapidly as the peak current grows while the phase predicted by HFM is close to FEM prediction at different peak current.

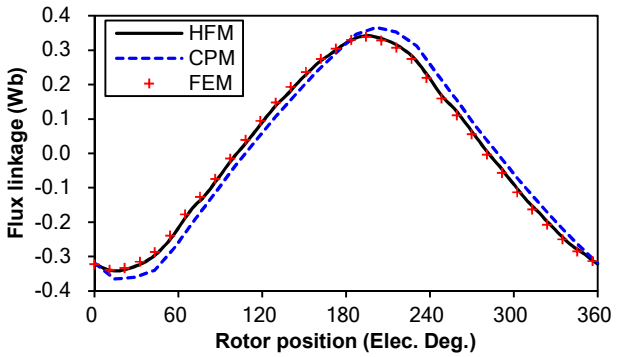

Fig. 14 HFM, CPM, and FEM predicted flux linkage waveforms of the 8-pole/48-slot SPM machine at rated current.

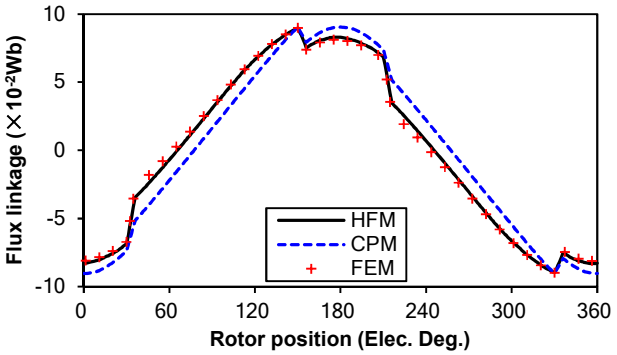

Fig. 15 HFM, CPM, and FEM predicted flux linkage waveforms of 8-pole/9-slot SPM machine at rated current.

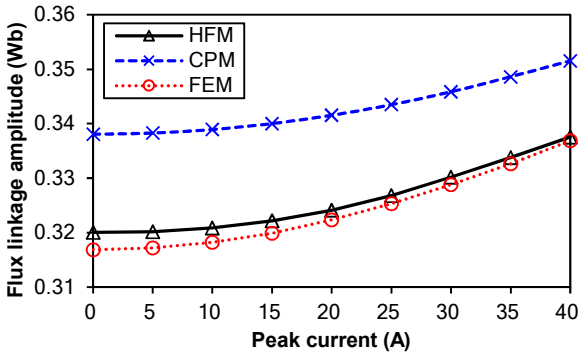

(a)

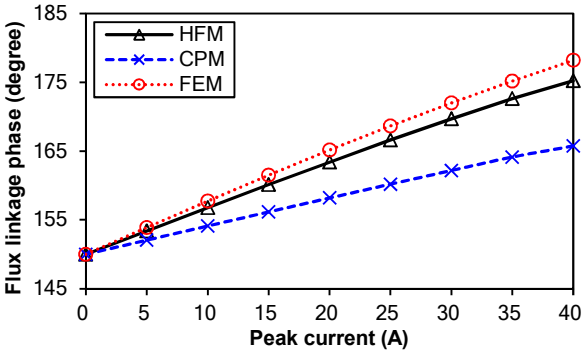

(b)

Fig. 16 Variation of amplitude and phase of the fundamental flux linkage with peak current of 8-pole/48-slot SPM machine: (a) amplitude and (b) phase.

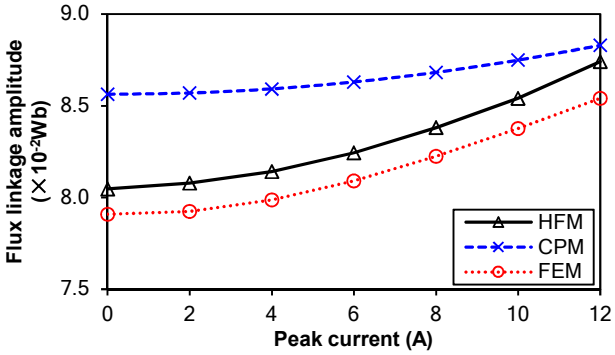

(a)

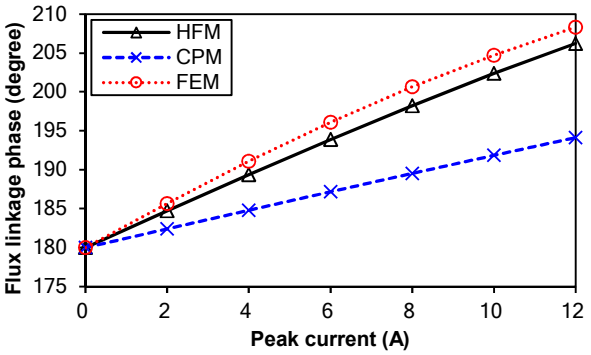

(b)

Fig. 17 Variation of amplitude and phase of the fundamental flux linkage with peak current of 8-pole/9-slot SPM machine: (a) amplitude and (b) phase.

Figs. 18-19 show that HFM has high accuracy for predicting the induced voltage waveform at rated current while CPM exhibits large errors for both machines. The induced voltage of 8-pole/9-slot machine from Fig. 19 has high surge voltage, because the current waveform in the simulation, Fig. 8(b), is ideal and has unsmooth changes. However, HFM consistently achieves good accuracy. Besides, the excellent accuracy of HFM can also be observed by the comparison of harmonic component of induced voltage in Figs. 20-21. Figs. 22-23 show the comparison between the HFM, CPM and FEM predictions of the amplitude and phase of the fundamental induced voltage at different peak current. Again, HFM can accurately predict the amplitude and phase of the fundamental induced voltage while CPM predicts higher amplitude of the fundamental induced voltage with larger phase error. Such advantages of HFM is attribute to its inclusion of flux leakage and saturation effect for predicting flux linkage and induced voltage.

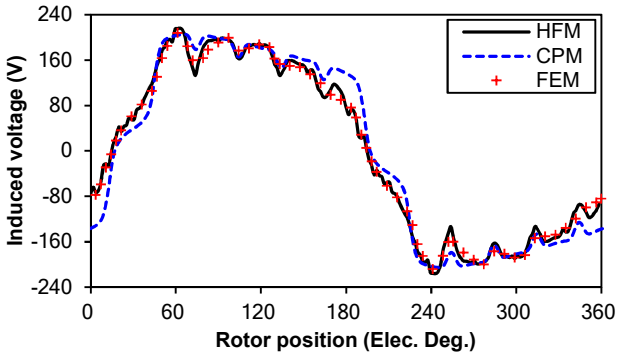

Fig. 18 HFM, CPM, and FEM predicted induced voltage waveforms of 8-pole/48-slot SPM machine at rated current.

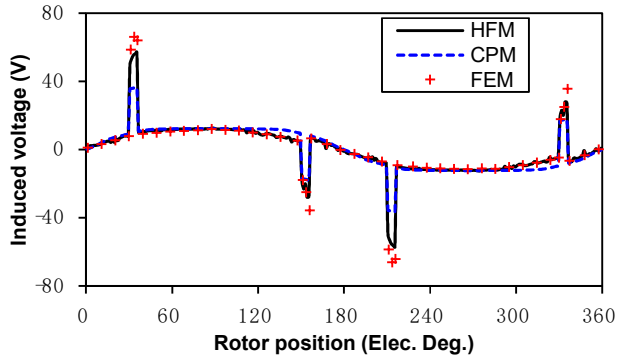

Fig. 19 HFM, CPM, and FEM predicted induced voltage waveforms of 8-pole/9-slot SPM machine at rated current.

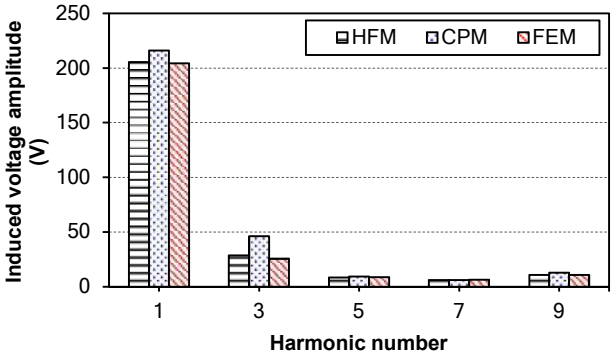

Fig. 20 Harmonic component of HFM, CPM, and FEM predicted induced voltage of 8-pole/48-slot SPM machine at rated current.

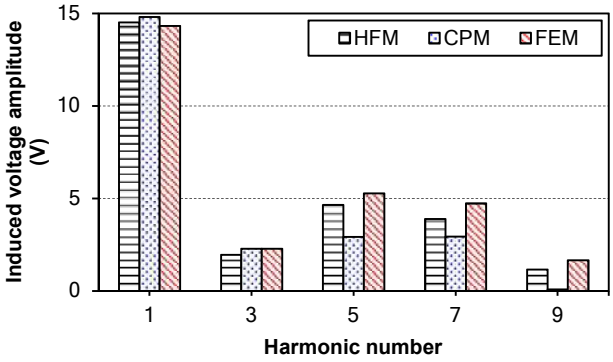

Fig. 21 Harmonic component of HFM, CPM, and FEM predicted induced voltage of 8-pole/9-slot SPM machine at rated current.

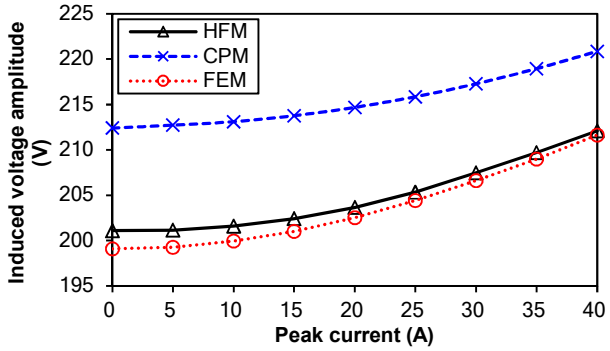

(a)

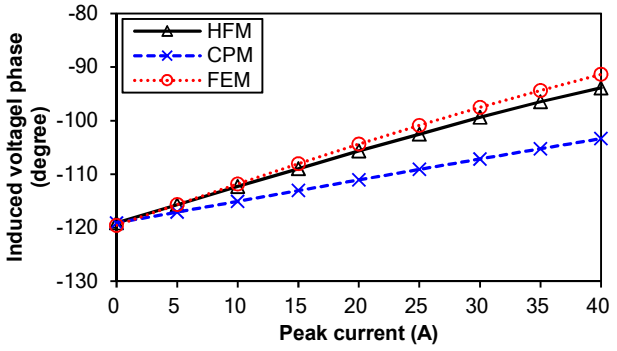

(b)

Fig. 22 Variation of amplitude and phase of the fundamental induced voltage with peak current of 8-pole/48-slot SPM machine: (a) amplitude and (b) phase.

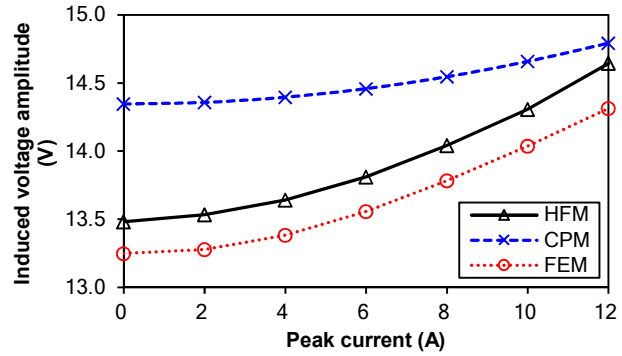

(a)

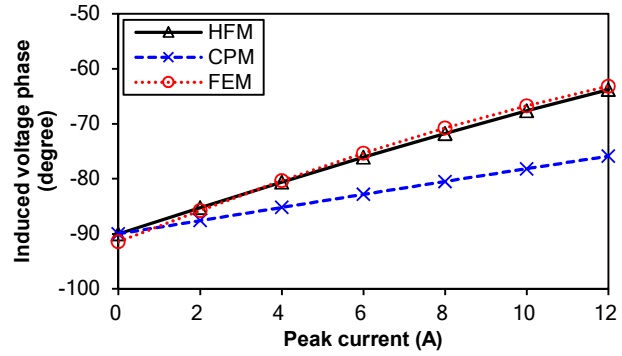

(b)

Fig. 23 Variation of amplitude and phase of the fundamental induced voltage with peak current of 8-pole/9-slot SPM machine: (a) amplitude and (b) phase.

Fig. 24 shows that the torque waveform predicted by HFM agrees well with FEM prediction at rated current while CPM overestimates it for 8-pole/48-slot machine. As for 8-pole/9-slot machine, the HFM prediction agrees well with both FEM and measured results while CPM always predicts higher torque waveform in Fig. 25. Moreover, as shown in Figs. 26-27, the average torque predicted by HFM achieves excellent accuracy at different load current while the error of CPM prediction gradually becomes larger with the increase of load.

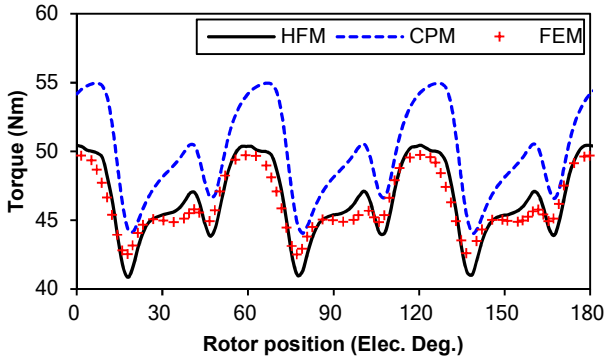

Fig. 24 HFM, CPM, and FEM predicted torque waveforms of 8-pole/48-slot SPM machine at rated current.

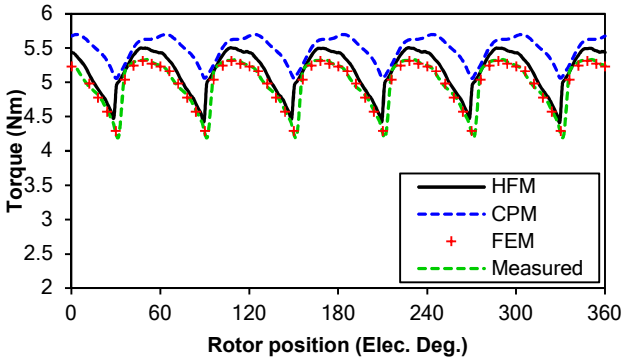

Fig. 25 HFM, CPM, FEM predicted torque waveforms and measured torque waveform of 8-pole/9-slot machine at rated current.

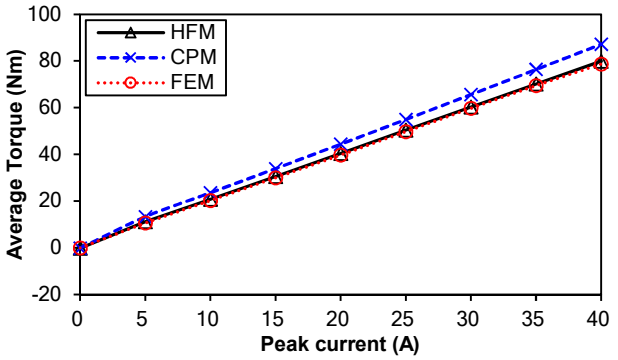

Fig. 26 Variation of average torque with peak current of 8-pole/48-slot SPM machine.

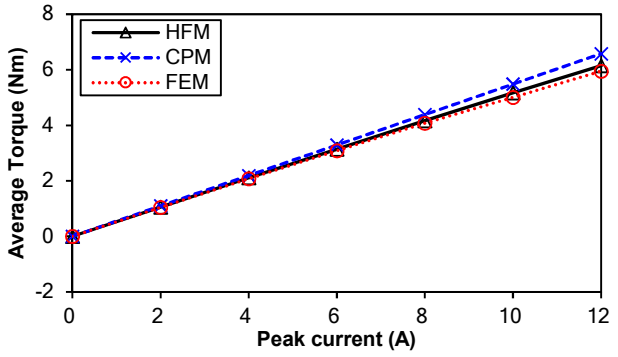

Fig. 27 Variation of average torque with peak current of 8-pole/9-slot SPM machine.

V. Conclusion

This paper has developed a hybrid field model for predicting

the on-load field and electromagnetic performance in SPM machines considering saturation effect. The saturation of the stator yoke and tooth body is represented by equivalent current on the slot while the tooth-tip saturation is accounted for by additional equivalent current sheet on the tooth surface. Based on such equivalent current sheets, the permeability of the iron can be regarded as infinite and superposition theory is applied to calculate the on-load air-gap field produced by PMs, winding current and equivalent current. In order to calculate the equivalent current, a solving procedure is introduced to guarantee the convergence. Then the air-gap field distribution, flux linkage, induced voltage and torque are all obtained from HFM. It can be seen that HFM has higher accuracy than CPM for predicting the air-gap field and electromagnetic performance due to considering saturation effect. Besides, both FEM predictions and experimental results demonstrates excellent accuracy of HFM.

APPENDIX

A. Field Produced by PM

The governing Laplacian equation in the air-gap region is [22]

$$\frac{\partial^2\varphi_I}{\partial r^2}+\frac{1}{r}\frac{\partial\varphi_I}{\partial r}+\frac{1}{r^2}\frac{\partial^2\varphi_I}{\partial\alpha^2}=0 \tag{40}$$

while the governing quasi-Poissonian equation in the permanent magnet region is

$$\frac{\partial^2\varphi_{II}}{\partial r^2}+\frac{1}{r}\frac{\partial\varphi_{II}}{\partial r}+\frac{1}{r^2}\frac{\partial^2\varphi_{II}}{\partial\alpha^2}=\frac{1}{\mu_r}div\overrightarrow{M} \tag{41}$$

The boundary condition in the air-gap region and permanent magnet region is

$$\begin{cases} H_{\alpha I}\big|_{r=R_s}=0 \\ H_{\alpha II}\big|_{r=R_r}=0 \\ B_{rI}\big|_{r=R_m}=B_{rII}\big|_{r=R_m} \\ H_{\alpha I}\big|_{r=R_m}=H_{\alpha II}\big|_{r=R_m} \end{cases} \tag{42}$$

The general solution of the air-gap field produced by PMs is shown in (13) and (14), where $K_B(n)$, $f_{Br}(r)$, and $f_{B\theta}(r)$ are given as:

when $np\neq 1$:

$$K_B(n)=\frac{\mu_0 M_n}{\mu_m}\frac{np}{(np)^2-1} *\frac{(A_{3n}-1)+2\left(\frac{R_r}{R_m}\right)^{np+1}-(A_{3n}+1)\left(\frac{R_r}{R_m}\right)^{2np}}{\frac{\mu_m+1}{\mu_m}\left[1-\left(\frac{R_r}{R_s}\right)^{2np}\right]-\frac{\mu_m-1}{\mu_m}\left[\left(\frac{R_m}{R_s}\right)^{2np}-\left(\frac{R_r}{R_m}\right)^{2np}\right]} \tag{43}$$

$$A_{3n}=\left(np-\frac{1}{np}\right)\frac{M_{rn}}{M_n}+\frac{1}{np} \tag{44}$$

$$f_{Br}(r)=\left(\frac{r}{R_s}\right)^{np-1}\left(\frac{R_m}{R_s}\right)^{np+1}+\left(\frac{R_m}{r}\right)^{np+1} \tag{45}$$

$$f_{B\theta}(\mathrm{r})=-\left(\frac{r}{R_s}\right)^{np-1}\left(\frac{R_m}{R_s}\right)^{np+1}+\left(\frac{R_m}{r}\right)^{np+1} \tag{46}$$

when np=1:

$$K_B(n)=\frac{\mu_0 M_n}{2\mu_m} *\frac{A_{3n}\left(\frac{R_m}{R_s}\right)^2-A_{3n}\left(\frac{R_r}{R_s}\right)^2+\left(\frac{R_r}{R_s}\right)^2\ln\left(\frac{R_m}{R_s}\right)^2}{\frac{\mu_m+1}{\mu_m}\left[1-\left(\frac{R_r}{R_s}\right)^2\right]-\frac{\mu_m-1}{\mu_m}\left[\left(\frac{R_m}{R_s}\right)^2-\left(\frac{R_r}{R_m}\right)^2\right]} \tag{47}$$

$$A_{3n}=2\frac{M_{r1}}{M_1}-1 \tag{48}$$

$$f_{Br}(r)=1+\left(\frac{R_s}{r}\right)^2 \tag{49}$$

$$f_{B\theta}(\mathrm{r})=-1+\left(\frac{R_s}{r}\right)^2 \tag{50}$$

where μ_m is the relative recoil permeability of the PM, p is the number of pole-pairs, where M_n is defined as

$$M_n=M_{rn}+npM_{\theta n} \tag{51}$$

where for radial magnetization

$$M_{rn}=2(B_r/\mu_0)\alpha_p\frac{\sin\frac{n\pi\alpha_p}{2}}{\frac{n\pi\alpha_p}{2}} \tag{52}$$

$$M_{\theta n}=0 \tag{53}$$

and for parallel magnetization

$$M_{rn}=\frac{B_{r0}}{\mu_0}\alpha_p(A_{1n}+A_{2n}) \tag{54}$$

$$M_{\theta n}=\frac{B_{r0}}{\mu_0}\alpha_p(A_{1n}-A_{2n}) \tag{55}$$

where

$$A_{1n}=\frac{\sin\left[(np+1)\alpha_p\frac{\pi}{2p}\right]}{(np+1)\alpha_p\frac{\pi}{2p}}$$

$$A_{2n}=\begin{cases} 1, & np=1 \\ \dfrac{\sin\left[(np-1)\alpha_p\frac{\pi}{2p}\right]}{(np-1)\alpha_p\frac{\pi}{2p}}, & np\neq 1 \end{cases} \tag{56}$$

where α is the stator angular position with reference to the axis of phase A winding, α_p is the magnet pole-arc to pole-pitch ratio and B_{r0} is the magnet remanence.

B. Slotting Effect

The complex permeance function is calculated using four conformal transformations [6]

$$Z=\ln r_a+j*\theta_a \tag{57}$$

$$Z = j\frac{g'}{\pi}\left[\ln\left(\frac{1+p}{1-p}\frac{b-p}{b+p}\right) - 2\frac{b-1}{\sqrt{b}}\tan^{-1}\frac{p}{\sqrt{b}}\right] + \ln R_s + j\theta_2 \quad (58)$$

$$p = \sqrt{\frac{w-b}{w-a}} \quad (59)$$

$$K = R_s e^{j(\frac{g'}{\pi}\ln w + \frac{\theta_s}{2})} \quad (60)$$

$$\lambda = \frac{K}{r_a e^{\theta_a}}\frac{\omega - 1}{\sqrt{(\omega - \mathrm{a})(\omega - \mathrm{b})}} = \lambda_r + j\lambda_i \quad (61)$$

where λ is the complex relative air-gap permeance, r_a and θ_a is the air-gap position of the machine in polar coordinates, θ_s=2π/Q_s, a and b are described as

$$b = \left[\frac{b_0}{2g'} + \sqrt{\left(\frac{b_0}{2g'}\right)^2 + 1}\right]^2 \quad (62)$$

$$a = \frac{1}{b} \quad (63)$$

$$g' = \ln\frac{R_s}{R_r} \quad (64)$$

where θ_2 is the angle of the slot corner.

REFERENCES

[1] Z. Q. Zhu and D. Howe, "Electrical machines and drives for electric, hybrid, and fuel cell vehicles," *Proc. IEEE*, vol. 95, no. 4, pp. 746-765, Apr. 2007.

[2] S. Ruoho, T. Santa-Nokki, J. Kolehmainen, and A. Arkkio, "Modeling magnet length in 2-D finite-element analysis of electric machines," *IEEE Trans. Magn*., vol. 45, no. 8, pp. 3114–3120, Aug. 2009.

[3] Z. Q. Zhu, D. Howe, E. Bolte, and B. Ackermann, "Instantaneous magnetic field distribution in brushless permanent magnet dc motors. Part I: open-circuit field," *IEEE Trans. Magn.,* vol. 29, no. 1, pp. 124–135, Jan. 1993.

[4] Z. Q. Zhu and D. Howe, "Instantaneous magnetic field distribution in brushless permanent magnet DC motors. II. armature-reaction field," *IEEE Trans. Magn.,* vol. 29, no. 1, pp. 136-142, Jan. 1993.

[5] Z. Q. Zhu and D. Howe, "Instantaneous magnetic field distribution in brushless permanent magnet DC motors. III. effect of stator slotting," *IEEE Trans. Magn.,* vol. 29, no. 1, pp. 143-151, Jan. 1993.

[6] D. Zarko, D. Ban, and T. A. Lipo, "Analytical calculation of magnetic field distribution in the slotted air gap of a surface permanent-magnet motor using complex relative air-gap permeance," *IEEE Trans. Magn.,* vol. 42, no. 7, pp. 1828-1837, July 2006.

[7] N. Boules, "Prediction of no-load flux density distribution in permanent magnet machines," *IEEE Trans. Ind. Appl.,* vol. IA-21, no. 3, pp. 633-643, May 1985.

[8] T. C. O'Connell and P. T. Krein, "A Schwarz-Christoffel-based analytical method for electric machine field analysis," *IEEE Trans. Energy Convers*., vol. 24, no. 3, pp. 565-577, Sept. 2009.

[9] K. Boughrara, R. Ibtiouen, D. Zarko, O. Touhami, and A. Rezzoug, "Magnetic field analysis of external rotor permanent-magnet synchronous motors using conformal mapping," *IEEE Trans. Magn.,* vol. 46, no. 9, pp. 3684-3693, Sept. 2010.

[10] L. J. Wu, Z. Q. Zhu, D. Staton, M. Popescu, and D. Hawkins, "An improved subdomain model for predicting magnetic field of surface-mounted permanent magnet machines accounting for tooth-tips," *IEEE Trans. Magn.,* vol. 47, no. 6, pp. 1693-1704, June 2011.

[11] A. Dalal and P. Kumar, "Analytical model for permanent magnet motor with slotting effect, armature reaction, and ferromagnetic material property," *IEEE Trans. Magn.,* vol. 51, no. 12, pp. 1-10, Dec. 2015.

[12] P. Liang, F. Chai, Y. Li, and Y. Pei, "Analytical prediction of magnetic field distribution in spoke-type permanent-magnet synchronous machines accounting for bridge saturation and magnet shape," *IEEE Trans. Ind. Electron.,* vol. 64, no. 5, pp. 3479-3488, May 2017.

[13] Z. Djelloul-Khedda, K. Boughrara, F. Dubas, and R. Ibtiouen, "Nonlinear analytical prediction of magnetic field and electromagnetic performances in switched reluctance machines," *IEEE Trans. Magn.,* vol. 53, no. 7, pp. 1-11, July 2017.

[14] M. Farshadnia, M. A. M. Cheema, R. Dutta, and J. E. Fletcher, "Analytical modeling of armature reaction air-gap flux density considering the non-homogeneously saturated rotor in a fractional-slot concentrated-wound IPM machine," *IEEE Trans. Magn*., vol. 53, no. 2, pp. 1-12, Feb. 2017.

[15] F. R. Alam and K. Abbaszadeh, "Magnetic field analysis in eccentric surface-mounted permanent-magnet motors using an improved conformal mapping method," *IEEE Trans. Energy Convers*., vol. 31, no. 1, pp. 333-344, March 2016.

[16] K. Abbaszadeh and F. Rezaee Alam, "On-load field component separation in surface-mounted permanent-magnet motors using an improved conformal mapping method," *IEEE Trans. Magn*., vol. 52, no. 2, pp. 1-12, Feb. 2016.

[17] F. Rezaee. Alam, B. Rezaeealam, and J. Faiz, "Unbalanced magnetic force analysis in eccentric surface permanent-magnet motors using an improved conformal mapping method," *IEEE Trans. Energy Convers*., vol. 32, no. 1, pp. 146-154, Mar. 2017.

[18] A. Hanic, D. Zarko, and Z. Hanic, "A novel method for no-load magnetic field analysis of saturated surface permanent-magnet machines using conformal mapping and magnetic equivalent circuits," *IEEE Trans. Energy Convers*., vol. 31, no. 2, pp. 740-749, Jun. 2016.

[19] A. Hanic, D. Zarko, D. Kuhinek, and Z. Hanic, "On-Load analysis of saturated surface permanent magnet machines using conformal mapping and magnetic equivalent circuits," *IEEE Trans. Energy Convers*., no. 99, pp. 1-1, Jan. 2018.

[20] L. J. Wu, Z. K. Li, X. Y. Huang, Y. L. Zhong, Y. T. Fang, and Z. Q. Zhu, "A hybrid field model for open-circuit field prediction in surface-mounted PM machines considering saturation," *IEEE Trans. Magn*., in press.

[21] V. Ostovic, *Dynamics of saturated electric machines*. New York, NY, USA: Springer-Verlag, 1989.

[22] Z. Q. Zhu, D. Howe, and C. C. Chan, "Improved analytical model for predicting the magnetic field distribution in brushless permanent-magnet machines," *IEEE Trans. Magn.,* vol. 38, no. 1, pp. 229-238, Jan 2002.

[23] D. Zarko, D. Ban, and T. A. Lipo, "Analytical solution for electromagnetic torque in surface permanent-magnet motors using conformal mapping," *IEEE Trans. Magn*., vol. 45, no. 7, pp. 2943-2954, July 2009.

[24] L. J. Wu, Z. Q. Zhu, D. A. Staton, M. Popescu, and D. Hawkins, "Comparison of analytical models of cogging torque in surface-mounted PM machines," *IEEE Trans. Ind. Electron.,* vol. 59, no. 6, pp. 2414-2425, June 2012.

[25] Z. Azar, Z. Q. Zhu, and G. Ombach, "Influence of electric loading and magnetic saturation on cogging torque, back-EMF and torque ripple of PM machines," *IEEE Trans. Magn.,* vol. 48, no. 10, pp. 2650-2658, Oct. 2012.

[26] Z. Q. Zhu and D. Howe, "Instantaneous magnetic field distribution in permanent magnet brushless DC motors. IV. magnetic field on load," *IEEE Trans. Magn.,* vol. 29, no. 1, pp. 152-158, Jan. 1993.